

Searching for the QCD critical endpoint using multi-point Padé approximations

D. A. Clarke,¹ P. Dimopoulos,² F. Di Renzo,² J. Goswami,³ C. Schmidt,⁴ S. Singh,⁴ and K. Zambello⁵

¹*Department of Physics and Astronomy, University of Utah, Salt Lake City, Utah, United States*

²*Dipartimento di Scienze Matematiche, Fisiche e Informatiche,*

Università di Parma and INFN, Gruppo Collegato di Parma I-43100 Parma, Italy

³*RIKEN Center for Computational Science, Kobe 650-0047, Japan*

⁴*Universität Bielefeld, Fakultät für Physik, D-33615 Bielefeld, Germany*

⁵*Dipartimento di Fisica dell'Università di Pisa and INFN-Sezione di Pisa, Largo Pontecorvo 3, I-56127 Pisa, Italy.*

(Dated: May 17, 2024)

Using the multi-point Padé approach, we locate Lee-Yang edge singularities of the QCD pressure in the complex baryon chemical potential plane. These singularities are extracted from singularities in the net baryon-number density calculated in $N_f = 2 + 1$ lattice QCD at physical quark mass and purely imaginary chemical potential. Taking an appropriate scaling ansatz in the vicinity of the conjectured QCD critical endpoint, we extrapolate the singularities on $N_\tau = 6$ lattices to pure real baryon chemical potential to estimate the position of the critical endpoint (CEP). We find $T^{\text{CEP}} = 105_{-18}^{+8}$ MeV and $\mu_B^{\text{CEP}} = 422_{-35}^{+80}$ MeV, which compares well with recent estimates in the literature. For the slope of the transition line at the critical point we find $-0.16(24)$.

PACS numbers: 11.10.Wx, 11.15.Ha, 12.38.Aw, 12.38.Gc, 12.38.Mh, 24.60.Ky, 25.75.Gz, 25.75.Nq

Introduction.—A central goal of the experimental program at the Relativistic Heavy-Ion Collider (RHIC) of Brookhaven National Laboratory (BNL) in the US and at the Large Hadron Collider (LHC) at CERN, Switzerland is the exploration of the phase diagram of quarks and gluons in the plane of temperature T and baryon chemical potential μ_B as described by the theory of the strong interaction, quantum chromodynamics (QCD). At low T and μ_B , QCD matter is known to exist as a gas of hadrons. At high T and/or μ_B , hadrons start to melt and quark-gluon plasma (QGP) is created. The QGP created at high μ_B may experience a sharp first-order phase transition as it cools, with bubbles of QGP and hadrons coexisting at a well-defined temperature. The coexistence region ends in a critical point (CEP), where QGP and hadronic matter become indistinguishable. The conjectured CEP belongs to the $3-d$, $Z(2)$ universality class.

Progress in understanding the phase diagram at $\mu_B > 0$ from first-principle lattice QCD calculations, in particular locating the CEP, is stymied by the infamous sign problem. In spite of this difficulty, lattice calculations are able to provide some controlled information of the diagram at sufficiently small μ_B/T . This is accomplished using various techniques, for instance reweighting [1, 2], analytic continuation from purely imaginary μ_B [3, 4], and Taylor expansion in μ_B/T [5, 6]. The Taylor expansion technique, while highly successful, is severely limited by the computational power required to compute higher-order Taylor coefficients, with state-of-the-art calculations achieving eighth order [7, 8]. In response to this challenge, various resummation schemes have been proposed [9–11], which all attempt to probe deeper into the phase diagram without having to compute even higher-order cumulants. Recently the STAR collaboration has found tantalizing evidence of the hint of a QCD critical

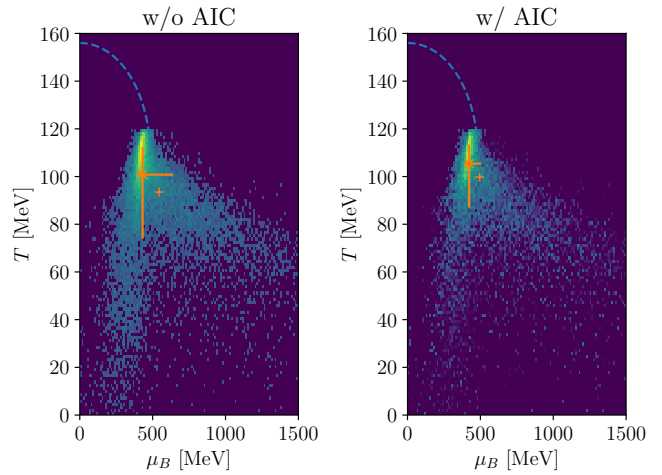


FIG. 1. Probability distribution of the QCD critical point from extrapolating Lee-Yang singularities to the real domain using universal scaling. For a detailed description see the text.

point [12] in the net proton fluctuation data. However, from the analysis of the QCD equation of state [13, 14] using Taylor expansion and Padé approximation, it is concluded that the CEP is likely not located in the energy range of the beam energy scan II (BESII) program at RHIC in collider mode.

In this paper we adopt the multi-point-Padé resummation method introduced in [15]. The method uses information from simulations at purely imaginary μ_B to construct a Padé approximation to the logarithm of the QCD grand partition function $\log \mathcal{Z}_{\text{QCD}}$ for complex μ_B . We then determine singularities of the approximant to estimate the CEP location. In particular we consider temperature-like and magnetization-like couplings t and h near the CEP. Then according to the Lee-Yang theo-

rem [16] applied to the universal theory (3-d $Z(2)$), at $t = 0$, zeroes of \mathcal{Z}_{QCD} in the complex h -plane that approach the real axis in the thermodynamic limit correspond to phase transitions. For $t > 0$, the closest singularities to the origin are the Lee-Yang edges (LYE). We extrapolate the position of the singularity to the the CEP by following LYE scaling [17].

From model calculations and model-independent symmetry arguments we understood that the location of T^{CEP} has to be searched below the chiral transition temperature $T_c^{\text{chiral}} \approx 132$ MeV [18]. Thus, we extend our calculations down to $T = 120$ MeV in this paper. Our final results are summarized in Fig. 1. We note that they are consistent with the bounds on T and μ_B mentioned above.

Lattice simulation details.—We generated configurations for a $N_\sigma^3 \times N_\tau$ lattice with $N_\sigma = 36$ and $N_\tau = 6$ and $N_f = 2 + 1$ dynamical highly improved staggered quarks (HISQ) [19] using the SIMULATEQCD [20, 21] implementation of the rational hybrid Monte Carlo algorithm (RHMC) [22]. We choose bare parameters along the line of constant physical pion mass obtained for the ratio of light to strange quark mass $m_s/m_l = 27$ in Refs. [23–25]. The simulations run at $\mathcal{O}(10)$ pure imaginary μ_B in the range $\mu_B/T \in [0, i\pi]$ to avoid the sign problem. For simplicity we set light and strange quark chemical potentials to equal values, $\mu_l = \mu_s$, which corresponds to baryon chemical potential $\mu_B = 3\mu_l$ and zero strangeness chemical potential $\mu_S = 0$. A number of configurations ranging from 1800 to 24000 was generated for a set of five temperatures ($T = 166.6, 157.5, 145.0, 136.1$ and 120.0 MeV) extending far below the chiral transition temperature as summarized in Table I. The configurations are separated by 10 molecular dynamic time units (MDTU).

We measured the first- and second-order cumulants of the net baryon-number density, defined as

$$\chi_n^B = \frac{N_\tau^3}{N_\sigma^3} \left(\frac{\partial}{\partial \mu_B} \right)^n \log \mathcal{Z}_{\text{QCD}}. \quad (1)$$

A total of 500 random vectors were used to construct unbiased noisy estimators of the observables. Numerical results are illustrated in Fig. 2. The first-order cumulant is a pure imaginary, odd, and 2π -periodic function of μ_B/T whose signal gets damped as the temperature is decreased. Conversely the second-order cumulant is a pure real, even, and 2π -periodic function of μ_B/T .

Mapping Poles of the multi-point Padé to Lee-Yang Edge singularities.—The first order cumulant is approximated by a rational function of the form

$$R_3^3(x) = \frac{\sum_{i=0}^3 a_i x^i}{1 + \sum_{i=1}^3 b_i x^i}. \quad (2)$$

In the generalized least square process [15], data of the

β	T [MeV]	N_μ	N_{conf}/N_μ
6.170	166.6	10	1800
6.120	157.5	10	4780
6.038	145.0	10	5300
5.980	136.1	10	6840
5.850	120.0	10	24000

TABLE I. Summary of statistics for each ensemble used in this study. The last column gives approximate number of thermalized configurations per μ value. Quark masses are fixed to their physical value and $\mu_s = \mu_l$.

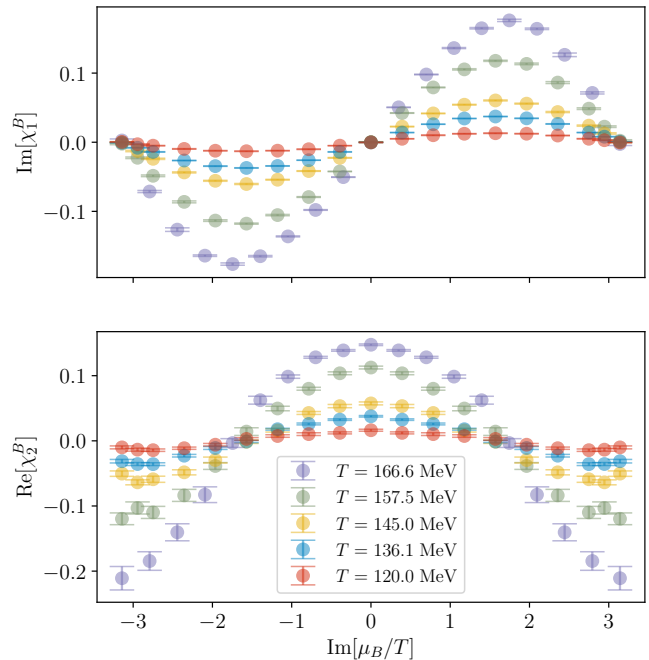


FIG. 2. First (top) and second (bottom) order net baryon-number cumulants at $T = 166.6, 157.5, 145.0, 136.1$ and 120.0 MeV. The points in the interval $[0, i\pi]$ are calculated, the points in $[-i\pi, 0]$ are obtained by reflection symmetry.

first two cumulants are taken into account. The fit interval $[\hat{\mu}_{\text{min}}, \hat{\mu}_{\text{max}}]$ is contained in $[-i\pi, +i\pi]$, and the length $\hat{\mu}_{\text{max}} - \hat{\mu}_{\text{min}}$ is varied between π and 2π . In this way we construct 55 rational approximations per temperature. We obtain the poles of the rational approximation by calculating the roots of the polynomial in the denominator. We keep only the roots in the first quadrant and pick the one which is closest to the center of our fit interval. For each fit interval and temperature we repeat the calculation of poles on $\mathcal{O}(200)$ samples, generated by bootstrapping over the standard deviation of the cumulant data. In this way we generate distributions of poles which we may represent as 1σ -confidence ellipses, as shown in Fig. 3 for a particular choice of intervals. We observe that the imaginary part of the poles decreases with decreasing temperature. The large error on the position of the $T = 166.6$ point is likely due to the much lower

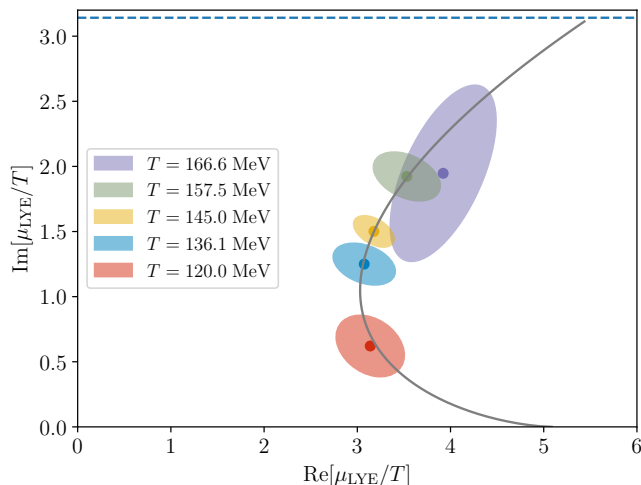


FIG. 3. Singularities at $T = 166.6, 157.5, 145.0, 136.1$ and 120.0 MeV. The dashed line lies at $\hat{\mu}_B = i\pi$.

number of gauge configurations as compared to the other points (see Table I). The solid grey line in Fig. 3 stems from the fit described below. We note that for $T > 170$ MeV, the poles accumulate on the dashed line in Fig. 3 and follow a scaling associated with the Roberge-Weiss transition in QCD [15, 26, 27].

Estimation of CEP location.—The QCD CEP is expected to belong to the 3- d , $Z(2)$ universality class. The mapping from the control parameters T and μ_B to the temperature-like and magnetization-like scaling directions t and h of the Ising model is not known. We thus adopt a frequently used linear ansatz for the mapping [28–31],

$$\begin{aligned} t &= A_t \Delta T + B_t \Delta \mu_B, \\ h &= A_h \Delta T + B_h \Delta \mu_B, \end{aligned} \quad (3)$$

with $\Delta T \equiv T - T^{\text{CEP}}$, $\Delta \mu_B \equiv \mu_B - \mu_B^{\text{CEP}}$, and constants A_i, B_i . For the extrapolation of the poles to the real axis, we would like to follow the path of the LYE. Expressed in terms of the scaling variable $z \equiv t/|h|^{1/\beta\delta}$, it has a constant position [17]

$$z_{\text{LYE}} = |z_{\text{LYE}}| e^{i\pi/2\beta\delta}. \quad (4)$$

Here β, δ are the well known critical exponents of the 3- d , $Z(2)$ universality class; we use the values $\beta = 0.326419$, $\delta = 4.78984$ [32]. For a discussion of the universal constant $|z_{\text{LYE}}|$ see [33–36]. Plugging eq. (3) into eq. (4) then implies that μ_{LYE} should scale [37] as

$$\begin{aligned} \text{Re } \mu_{\text{LYE}} &= \mu_B^{\text{CEP}} + c_1 \Delta T + c_2 \Delta T^2 + O(\Delta T^3) \\ \text{Im } \mu_{\text{LYE}} &= c_3 \Delta T^{\beta\delta}, \end{aligned} \quad (5)$$

where the coefficients c_i are functions of the mixing parameters A_j, B_j . In particular we have $c_1 = A_h/B_h$,

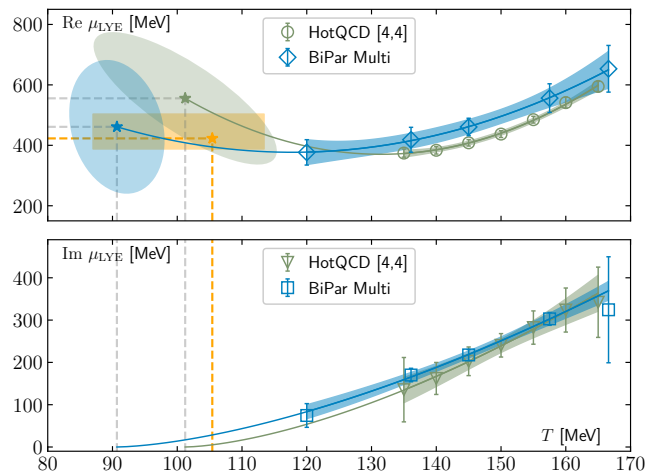


FIG. 4. Scaling fits for the LYE singularities related to the CEP. Green data come from a [4,4] Padé from Ref. [7]. Blue data come from the multi-point Padé. *Top*: Scaling of the real part. *Bottom*: Scaling of the imaginary part. The ellipses shown in the top panel represent the 68% confidence region deduced from the covariance matrix of the fit. The orange box indicates the AIC weighted estimate (6).

which denotes the slope of the transition line at the CEP in the (T, μ_B) -diagram. Note that the presence of the coefficient c_2 goes beyond the linear ansatz of eq. (3) but seems important to extrapolate our current data.

We use eq. (5) to simultaneously fit the real and imaginary parts of our singularities. In total the fit has 5 parameters, $\mu_B^{\text{CEP}}, T^{\text{CEP}}, c_1, c_2$, and c_3 . We checked that separate fits to real and imaginary parts give very similar results with slightly reduced errors.

Results for the CEP.—We perform $\mathcal{O}(10^5)$ different fits by varying the rational approximation for each temperature, based on different intervals and bootstrapping over the data. The results for the coordinates of the CEP are presented in Fig. 1 as a histogram, weighted with (right) and without (left) the Akaike information criterion (AIC). The median and the 68% confidence interval is estimated and presented in Fig. 1 by star symbols and error bars. In the AIC-weighted case we find

$$(T^{\text{CEP}}, \mu_B^{\text{CEP}}) = (105_{-18}^{+8}, 422_{-35}^{+80}) \text{ MeV}, \quad (6)$$

where the errors are statistical errors only. The plus symbols represent the arithmetic mean. Also plotted in Fig. 1 as a blue, dashed line is the crossover temperature. It is interesting to note that the histograms indicate two branches in the tails of the distribution. Whether these branches contain further information on the QCD phase diagram, e.g. on binodal or spinodal lines, will be interesting to discuss in future publications.

In order to compare the $N_\tau = 6$ results from imaginary chemical potential calculations with the eighth-order Taylor expansion results from $N_\tau = 8$ [7], the fit

with the best (smallest) $\chi^2/\text{d.o.f.}$ is presented in Fig. 4 (and Fig. 3). The same fit is applied to the singularities extracted from the [4,4]-Padé resummation of the pressure expansion presented in [7]. The blue and green ellipses drawn in Fig. 4 are the 68%-confidence ellipses obtained from the covariance matrix of the fit parameters. The orange square gives the estimate of the AIC-weighted median over all $N_\tau = 6$ fits. The error bands on the fit are obtained with error propagation implemented in the AnalysisToolbox [38], which is also used to carry out the fits. Data points and fits of $N_\tau = 6$ and $N_\tau = 8$ calculations are compatible within errors; the extrapolated location of the CEP might, however, give rise to some cutoff effects. The fit parameters are summarized in Table II.

Besides the location of the CEP, we can also estimate the slope of the transition line at the CEP. In the μ_B, T -diagram, the slope is given as $1/c_1 = -0.16(24)$. Since the direction of the temperature-like scaling field t is tangential to the transition line at the CEP, we can also estimate the angles between the t -axis and the axes of the μ_B, T -diagram.

$$\angle(t, T) = 80.8^\circ \pm 13.4^\circ \quad \angle(t, \mu_B) = 9.2^\circ \pm 13.4^\circ. \quad (7)$$

We note that the map in eq. (3) can be decomposed into translation, rotations and scales. In this case one of the above angles enters directly the mapping between the QCD parameter and the scaling fields.

Discussion.—An important consistency check for our results on the CEP location is the comparison with the crossover line. A natural parametrization of the pseudo-critical temperature T_{pc} is given as

$$T_{pc}(\mu_B) = T_{pc,0} \left(1 - \kappa_2 f^2(\mu_B) + \kappa_4 f^4(\mu_B) - \kappa_6 f^6(\mu_B) + \dots \right), \quad (8)$$

where $T_{pc,0} = 156.5(1.5)$ MeV is the crossover temperature at $\mu_B = 0$ and $f(\mu_B) = \mu_B/T$. In recent lattice QCD and other calculations, continuum extrapolated results for the curvature coefficients κ_2 and κ_4 were presented and remarkably agreement was found at least for $\mathcal{O}(\mu_B^2)$: $\kappa_2 = 0.15(1)$ (for the case $\mu_S = 0$) [39–45]. Note that frequently the crossover line is also parametrized with $f(\mu_B) = \mu_B/T_{pc,0}$ and coefficients $\bar{\kappa}_2, \bar{\kappa}_4$. We can map one parametrization to the other by setting $\bar{\kappa}_2 = \kappa_2$ and $\bar{\kappa}_4 = \kappa_4 - 2\kappa_2\bar{\kappa}_2$, with differences remaining at $\mathcal{O}(\mu_B^6)$. Our CEP location for $N_\tau = 6$ is roughly in agreement with the $\mathcal{O}(\mu_B^2)$ parametrization in $f(\mu_B) = \mu_B/T$. This parametrization is shown in Fig. 1 as dashed line. However, in the region where the CEP is located the contribution of the $\mathcal{O}(\mu_B^4)$ coefficient would already be significant, i.e. the two $\mathcal{O}(\mu_B^2)$ parametrizations with $f(\mu_B) = \mu_B/T$ and $f(\mu_B) = \mu_B/T_{pc,0}$ differ substantially for $\mu_B > 400$ MeV or $T < 140$ MeV. Plugging μ_B^{CEP} or T^{CEP} into the latter, would increase T^{CEP} or μ_B^{CEP} respectively. We note that current cutoff effects

that we observe between $N_\tau = 6$ and $N_\tau = 8$ calculations would lead to a continuum result of $(\mu_B^{\text{CEP}}, T^{\text{CEP}})$ that is consistent with $\bar{\kappa}_4 \approx 0$, which is favored by lattice calculations. Current estimates give $\bar{\kappa}_4 \approx 0.001(7)$ (again for $\mu_S = 0$) [39]. More precisely the value of μ_B^{CEP} would increase to $\mu_B^{\text{CEP}} \approx 650$ MeV. The reason why we are not seriously attempting to perform the continuum extrapolation here is that the $N_\tau = 6$ and $N_\tau = 8$ calculations differ by their methodology and might suffer from different systematic effects.

Our estimate for the CEP location (at least when taking cutoff effects into account) compares favorably with a number of other results and constraints. To begin with, it ought to lie outside the estimated convergence region of the Taylor series for $\log \mathcal{Z}_{\text{QCD}}$, i.e. it is expected¹ that $\mu_B/T \gtrsim 2$ [7, 46–48]. Moreover, if the CEP exists, it is expected to occur at a lower temperature than the chiral transition temperature [49], which is known to be 132^{+3}_-6 MeV [18]. Our estimate conforms to both of these expectations. Additionally it is in rough agreement with recent predictions from Dyson-Schwinger equations [44, 50], the functional renormalization group [43], and black-hole engineering [51]. Similar to our approach, the conformal Padé applied to the same HotQCD data yields a compatible result as well [52].

An important limitation of the estimates presented here² is that they are not fully extrapolated to the continuum limit. For the multi-point Padé, we are limited to $N_\tau = 6$, and the HotQCD data utilize χ_6^B and χ_8^B on $N_\tau = 8$ lattices. At this stage, it appears clear that both data sets are sensitive to a non-trivial singularity structure in μ_B that is consistent with Lee-Yang edge scaling, but in principle our estimates of the location of μ_B^{CEP} are distorted by cutoff effects.

Summary.—Here we present a new strategy for the critical point search at $\mu_B > 0$ by means of first principle lattice QCD calculations. Based on rational function approximations of the cumulants of the baryon-number fluctuations at imaginary chemical potential we determine singularities in the complex μ_B plane. We extrapolate these singularities using a scaling ansatz motivated by the temperature scaling of the Lee-Yang edge singularity. The rational function approximations are obtained by a multi-point Padé analysis on a sliding interval embedded in $\mu_B/T \in [-i\pi, i\pi]$. For the $N_\tau = 6$ results we find $T^{\text{CEP}} = 105^{+8}_{-18}$ MeV and $\mu_B^{\text{CEP}} = 422^{+80}_{-35}$ MeV, based on $\mathcal{O}(10^5)$ different fits. However we expect that cutoff effects will alter μ_B^{CEP} towards larger values of around ~ 650 MeV. This estimate is roughly consistent

¹ Strictly speaking, this estimate of the convergence radius depends on e.g. the temperature. Some of these earlier estimates come from coarse lattices. Still, they indicate convergence in the same general regime.

² And therefore also for Ref. [52].

	$N_\tau = 6$			$N_\tau = 8$		
	multi-point Padé			[4,4]-Padé		
	T^{CEP} [MeV]	μ_B^{CEP} [MeV]	μ_B/T	T^{CEP} [MeV]	μ_B^{CEP} [MeV]	μ_B/T
best fit	90.7 ± 7.7	461.2 ± 220	5.09 ± 0.68	101 ± 15	560 ± 140	5.5 ± 1.7
weight-1	$105.4 + 8.0 - 18.4$	$422.9 + 80.5 - 34.9$	$3.92 + 1.52 - 0.24$			
weight-2	$100.8 + 11.6 - 26.8$	$430.9 + 208.2 - 42.2$	$4.20 + 4.13 - 0.47$			
	c_1	c_2	c_3	c_1	c_2	c_3
best fit	-6.2 ± 9.2	0.115 ± 0.090	0.424 ± 0.086	-12.3 ± 8.1	0.203 ± 0.059	0.55 ± 0.25

TABLE II. Obtained fit parameters from the fit with eq. (5) to the real and imaginary parts of the singularities of $\log Z$. For $N_\tau = 6$, we show the results for the fit with the smallest $\chi^2/\text{d.o.f.}$ (0.067), as well as the median and 1σ -percentiles of all performed fits, weighted with (weight-1) and without (weight-2) the AIC.

with other estimates in the literature and also with the current determination of the crossover line.

Acknowledgement.—This work was supported by the Deutsche Forschungsgemeinschaft (DFG, German Research Foundation) Proj. No. 315477589-TRR 211, by the PUNCH4NFDI consortium supported by the Deutsche Forschungsgemeinschaft (DFG, German Research Foundation) with project number 460248186 (PUNCH4NFDI) and by INFN (Istituto Nazionale di Fisica Nucleare) under research project *i.s. QCDLAT*. In its early phase this work also received funding from the European Union’s Horizon 2020 research and innovation programme under the Marie Skłodowska-Curie grant agreement No. 813942 (*EuroPLEx*). Numerical calculations have been made possible through EuroHPC JU and PRACE grants at CINECA, Italy on Leonardo and Marconi100, and through the Gauss Centre for Supercomputing e.V. (www.gauss-centre.eu) on the GCS Supercomputer JUWELS [53] at Jülich Supercomputing Centre (JSC). Additional calculations have been performed on Leonardo under the INFN-CINECA agreement for HPC and on the GPU clusters at Bielefeld University, Germany. We also acknowledge support of the Bielefeld NPC.NRW team. DAC was supported by the National Science Foundation under Grant PHY20-13064. KZ acknowledges support by the project “Non-perturbative aspects of fundamental interactions, in the Standard Model and beyond” funded by MUR, Progetti di Ricerca di Rillevante Interesse Nazionale (PRIN), Bando 2022, Grant 2022TJFCYB (CUP I53D23001440006).

- [1] I. M. Barbour, S. E. Morrison, E. G. Klepfish, J. B. Kogut, and M.-P. Lombardo, Results on finite density QCD, Nuclear Physics B - Proceedings Supplements **60**, 220 (1998).
- [2] Z. Fodor and S. Katz, A new method to study lattice QCD at finite temperature and chemical potential, Physics Letters B **534**, 87 (2002).
- [3] P. de Forcrand and O. Philipsen, The QCD phase

diagram for small densities from imaginary chemical potential, Nucl. Phys. B **642**, 290 (2002), arXiv:hep-lat/0205016.

- [4] M. D’Elia and M.-P. Lombardo, Finite density QCD via imaginary chemical potential, Phys. Rev. D **67**, 014505 (2003), arXiv:hep-lat/0209146.
- [5] R. V. Gavai and S. Gupta, Pressure and nonlinear susceptibilities in QCD at finite chemical potentials, Phys. Rev. D **68**, 034506 (2003), arXiv:hep-lat/0303013.
- [6] C. R. Allton, M. Doring, S. Ejiri, S. J. Hands, O. Kaczmarek, F. Karsch, E. Laermann, and K. Redlich, Thermodynamics of two flavor QCD to sixth order in quark chemical potential, Phys. Rev. D **71**, 054508 (2005), arXiv:hep-lat/0501030.
- [7] D. Bollweg, J. Goswami, O. Kaczmarek, F. Karsch, S. Mukherjee, P. Petreczky, C. Schmidt, and P. Scior (HotQCD), Taylor expansions and Padé approximants for cumulants of conserved charge fluctuations at nonvanishing chemical potentials, Phys. Rev. D **105**, 074511 (2022), arXiv:2202.09184 [hep-lat].
- [8] S. Borsanyi, Z. Fodor, J. N. Guenther, S. K. Katz, K. K. Szabo, A. Pasztor, I. Portillo, and C. Ratti, Higher order fluctuations and correlations of conserved charges from lattice QCD, JHEP **10**, 205, arXiv:1805.04445 [hep-lat].
- [9] S. Borsányi, Z. Fodor, J. N. Guenther, R. Kara, S. D. Katz, P. Parotto, A. Pásztor, C. Ratti, and K. K. Szabó, Lattice QCD equation of state at finite chemical potential from an alternative expansion scheme, Phys. Rev. Lett. **126**, 232001 (2021), arXiv:2102.06660 [hep-lat].
- [10] S. Mondal, S. Mukherjee, and P. Hegde, Lattice QCD Equation of State for Nonvanishing Chemical Potential by Resumming Taylor Expansions, Phys. Rev. Lett. **128**, 022001 (2022), arXiv:2106.03165 [hep-lat].
- [11] S. Mitra, P. Hegde, and C. Schmidt, New way to resum the lattice QCD Taylor series equation of state at finite chemical potential, Phys. Rev. D **106**, 034504 (2022), arXiv:2205.08517 [hep-lat].
- [12] J. Adam *et al.* (STAR), Nonmonotonic Energy Dependence of Net-Proton Number Fluctuations, Phys. Rev. Lett. **126**, 092301 (2021), arXiv:2001.02852 [nucl-ex].
- [13] D. Bollweg, D. A. Clarke, J. Goswami, O. Kaczmarek, F. Karsch, S. Mukherjee, P. Petreczky, C. Schmidt, and S. Sharma (HotQCD), Equation of state and speed of sound of (2+1)-flavor QCD in strangeness-neutral matter at nonvanishing net baryon-number density, Phys. Rev. D **108**, 014510 (2023), arXiv:2212.09043 [hep-lat].
- [14] J. Goswami (HotQCD), The isentropic equation of state

- of (2+1)-flavor QCD: An update based on high precision Taylor expansion and Pade-resummed expansion at finite chemical potentials, PoS **LATTICE2022**, 149 (2023), arXiv:2212.10016 [hep-lat].
- [15] P. Dimopoulos, L. Dini, F. Di Renzo, J. Goswami, G. Nicotra, C. Schmidt, S. Singh, K. Zambello, and F. Ziesché, Contribution to understanding the phase structure of strong interaction matter: Lee-Yang edge singularities from lattice QCD, Phys. Rev. D **105**, 034513 (2022), arXiv:2110.15933 [hep-lat].
- [16] C.-N. Yang and T. D. Lee, Statistical theory of equations of state and phase transitions. 1. Theory of condensation, Phys. Rev. **87**, 404 (1952).
- [17] M. E. Fisher, Yang-Lee Edge Singularity and ϕ^3 Field Theory, Phys. Rev. Lett. **40**, 1610 (1978).
- [18] H. T. Ding *et al.* (HotQCD), Chiral Phase Transition Temperature in (2+1)-Flavor QCD, Phys. Rev. Lett. **123**, 062002 (2019), arXiv:1903.04801 [hep-lat].
- [19] E. Follana, Q. Mason, C. Davies, K. Hornbostel, G. P. Lepage, J. Shigemitsu, H. Trotter, and K. Wong (HPQCD, UKQCD), Highly improved staggered quarks on the lattice, with applications to charm physics, Phys. Rev. D **75**, 054502 (2007), arXiv:hep-lat/0610092.
- [20] L. Altenkort, D. Bollweg, D. A. Clarke, O. Kaczmarek, L. Mazur, C. Schmidt, P. Scior, and H.-T. Shu, HotQCD on multi-GPU Systems, PoS **LATTICE2021**, 196 (2022), arXiv:2111.10354 [hep-lat].
- [21] L. Mazur *et al.* (HotQCD), SIMULATEQCD: A simple multi-GPU lattice code for QCD calculations, Comput. Phys. Commun. **300**, 109164 (2024), arXiv:2306.01098 [hep-lat].
- [22] M. A. Clark and A. D. Kennedy, Accelerating dynamical fermion computations using the rational hybrid Monte Carlo (RHMC) algorithm with multiple pseudofermion fields, Phys. Rev. Lett. **98**, 051601 (2007), arXiv:hep-lat/0608015.
- [23] A. Bazavov *et al.*, The chiral and deconfinement aspects of the QCD transition, Phys. Rev. D **85**, 054503 (2012), arXiv:1111.1710 [hep-lat].
- [24] A. Bazavov *et al.* (HotQCD), Equation of state in (2+1)-flavor QCD, Phys. Rev. D **90**, 094503 (2014), arXiv:1407.6387 [hep-lat].
- [25] D. Bollweg, J. Goswami, O. Kaczmarek, F. Karsch, S. Mukherjee, P. Petreczky, C. Schmidt, and P. Scior (HotQCD), Second order cumulants of conserved charge fluctuations revisited: Vanishing chemical potentials, Phys. Rev. D **104**, 074512 (2021), arXiv:2107.10011 [hep-lat].
- [26] D. A. Clarke, K. Zambello, P. Dimopoulos, F. Di Renzo, J. Goswami, G. Nicotra, C. Schmidt, and S. Singh, Determination of Lee-Yang edge singularities in QCD by rational approximations, PoS **LATTICE2022**, 164 (2023), arXiv:2301.03952 [hep-lat].
- [27] C. Schmidt, D. A. Clarke, P. Dimopoulos, F. Di Renzo, J. Goswami, S. Singh, V. V. Skokov, and K. Zambello, Universal scaling and the asymptotic behaviour of Fourier coefficients of the baryon-number density in QCD, in *40th International Symposium on Lattice Field Theory* (2024) arXiv:2401.07790 [hep-lat].
- [28] J. J. Rehr and N. D. Mermin, Revised Scaling Equation of State at the Liquid-Vapor Critical Point, Phys. Rev. A **8**, 472 (1973).
- [29] C. Nonaka and M. Asakawa, Hydrodynamical evolution near the QCD critical end point, Phys. Rev. C **71**, 044904 (2005), arXiv:nucl-th/0410078.
- [30] P. Parotto, M. Bluhm, D. Mroczek, M. Nahrgang, J. Noronha-Hostler, K. Rajagopal, C. Ratti, T. Schäfer, and M. Stephanov, QCD equation of state matched to lattice data and exhibiting a critical point singularity, Phys. Rev. C **101**, 034901 (2020), arXiv:1805.05249 [hep-ph].
- [31] M. Kahangirwe, S. A. Bass, E. Bratkovskaya, J. Jahan, P. Moreau, P. Parotto, D. Price, C. Ratti, O. Soloveva, and M. Stephanov, Finite density QCD equation of state: critical point and lattice-based T' -expansion, (2024), arXiv:2402.08636 [nucl-th].
- [32] S. El-Showk, M. F. Paulos, D. Poland, S. Rychkov, D. Simmons-Duffin, and A. Vichi, Solving the 3d Ising Model with the Conformal Bootstrap II. c-Minimization and Precise Critical Exponents, J. Stat. Phys. **157**, 869 (2014), arXiv:1403.4545 [hep-th].
- [33] A. Connelly, G. Johnson, F. Rennecke, and V. Skokov, Universal Location of the Yang-Lee Edge Singularity in $O(N)$ Theories, Phys. Rev. Lett. **125**, 191602 (2020), arXiv:2006.12541 [cond-mat.stat-mech].
- [34] F. Rennecke and V. V. Skokov, Universal location of Yang-Lee edge singularity for a one-component field theory in $1 \leq d \leq 4$, Annals Phys. **444**, 169010 (2022), arXiv:2203.16651 [hep-ph].
- [35] G. Johnson, F. Rennecke, and V. V. Skokov, Universal location of Yang-Lee edge singularity in classic $O(N)$ universality classes, Phys. Rev. D **107**, 116013 (2023), arXiv:2211.00710 [hep-ph].
- [36] F. Karsch, C. Schmidt, and S. Singh, Lee-Yang and Langer edge singularities from analytic continuation of scaling functions, Phys. Rev. D **109**, 014508 (2024), arXiv:2311.13530 [hep-lat].
- [37] M. A. Stephanov, QCD critical point and complex chemical potential singularities, Phys. Rev. D **73**, 094508 (2006), arXiv:hep-lat/0603014.
- [38] L. Altenkort, D. A. Clarke, J. Goswami, and H. Sandmeyer, Streamlined data analysis in Python, *40th International Symposium on Lattice Field Theory*, PoS **LATTICE2023**, 136 (2023), arXiv:2308.06652 [hep-lat].
- [39] A. Bazavov *et al.* (HotQCD), Chiral crossover in QCD at zero and non-zero chemical potentials, Phys. Lett. B **795**, 15 (2019), arXiv:1812.08235 [hep-lat].
- [40] S. Borsanyi, Z. Fodor, J. N. Guenther, R. Kara, S. D. Katz, P. Parotto, A. Pasztor, C. Ratti, and K. K. Szabo, QCD Crossover at Finite Chemical Potential from Lattice Simulations, Phys. Rev. Lett. **125**, 052001 (2020), arXiv:2002.02821 [hep-lat].
- [41] R. Bellwied, S. Borsanyi, Z. Fodor, J. Günther, S. D. Katz, C. Ratti, and K. K. Szabo, The QCD phase diagram from analytic continuation, Phys. Lett. B **751**, 559 (2015), arXiv:1507.07510 [hep-lat].
- [42] C. Bonati, M. D'Elia, F. Negro, F. Sanfilippo, and K. Zambello, Curvature of the pseudocritical line in QCD: Taylor expansion matches analytic continuation, Phys. Rev. D **98**, 054510 (2018), arXiv:1805.02960 [hep-lat].
- [43] W.-j. Fu, J. M. Pawłowski, and F. Rennecke, QCD phase structure at finite temperature and density, Phys. Rev. D **101**, 054032 (2020), arXiv:1909.02991 [hep-ph].
- [44] F. Gao and J. M. Pawłowski, Chiral phase structure and critical end point in QCD, Phys. Lett. B **820**, 136584 (2021), arXiv:2010.13705 [hep-ph].
- [45] M. S. Ali, D. Biswas, A. Jaiswal, and H. Mishra, Effects

- of strangeness on the chiral pseudo-critical line, (2024), arXiv:2403.11965 [nucl-th].
- [46] M. Giordano and A. Pásztor, Reliable estimation of the radius of convergence in finite density QCD, *Phys. Rev. D* **99**, 114510 (2019), arXiv:1904.01974 [hep-lat].
- [47] M. Giordano, K. Kapas, S. D. Katz, D. Negradi, and A. Pasztor, Radius of convergence in lattice QCD at finite μ_B with rooted staggered fermions, *Phys. Rev. D* **101**, 074511 (2020), [Erratum: *Phys.Rev.D* 104, 119901 (2021)], arXiv:1911.00043 [hep-lat].
- [48] S. Mukherjee and V. Skokov, Universality driven analytic structure of the QCD crossover: radius of convergence in the baryon chemical potential, *Phys. Rev. D* **103**, L071501 (2021), arXiv:1909.04639 [hep-ph].
- [49] F. Karsch, Critical behavior and net-charge fluctuations from lattice QCD, *PoS CORFU2018*, 163 (2019), arXiv:1905.03936 [hep-lat].
- [50] P. J. Gunkel and C. S. Fischer, Locating the critical endpoint of QCD: Mesonic backcoupling effects, *Phys. Rev. D* **104**, 054022 (2021), arXiv:2106.08356 [hep-ph].
- [51] M. Hippert *et al.*, Bayesian location of the QCD critical point from a holographic perspective, 2309.00579 (2023).
- [52] G. Basar, On the QCD critical point, Lee-Yang edge singularities and Pade resummations, 2312.06952 (2023).
- [53] Jülich Supercomputing Centre, JUWELS Cluster and Booster: Exascale Pathfinder with Modular Supercomputing Architecture at Juelich Supercomputing Centre, *Journal of large-scale research facilities* **7**, 10.17815/jlsrf-7-183 (2021).

SUPPLEMENTAL MATERIAL

The sliding window analysis of the rational function approximation.—As we had already observed in Ref. [15], there is an interval dependence for the poles located by multi-point Padé analysis. When we change the interval we become more sensitive to some singularities and less to others. In particular we observe that for symmetric intervals centered at $\mu_B/T = i\pi$, thermal singularities that belong to the Roberge-Weiss transition are favored. For that reason we perform a very general sliding window analysis where we vary the interval length as well as the center of the interval used in the rational approximation. The length is varied between π and 2π , whereas the center of the interval is located in $[-i\pi/2, i\pi/2]$. Note that only the points between 0 and $i\pi$ are calculated. In other regions the data is duplicated through reflection symmetry and periodicity. The procedure is visualized in Fig. 5, for the example of the $T = 120$ MeV data and can be summarized by the following algorithm:

Algorithm 1: sliding window analysis

```

begin
  ClearData( $M, E$ );
  for  $i \in N_{\text{interval}}$  do
     $I_i \leftarrow \text{SelectInterval}(i)$ ;
    ClearData( $D, R, S$ );
    for  $j \in N_{\text{samples}}$  do
       $D_j \leftarrow \text{DrawBootstrapSample}(I_i)$ ;
       $R_j \leftarrow \text{RationalApproximation}(D_j)$ ;
       $S_j \leftarrow \text{CalcSingularities}(R_j)$ ;
     $M_i \leftarrow \text{CalcMean}(S)$ ;
     $E_i \leftarrow \text{CalcError}(S)$ ;

```

The subroutine `SelectInterval(i)` is chosen to be deterministic. We number all possible combinations of interval length and center in the above mentioned ranges that are possible with our data points. We find $N_{\text{interval}} = 55$. The subroutine `DrawBootstrapSample(I_i)` on the other hand assumes independent and normal distributed errors on the data points that have support in the interval I_i . The subroutine `RationalApproximation(D_j)` performs a combined fit to the χ_1^B and χ_2^B data from the sample D_j . We use the rational function $R_3^3(x)$ as given in eq. (2). We checked that higher order rational approximations give very similar results, however, the initial set of parameters for these fits have to be chosen more carefully to ensure convergence, and cancellations of poles in the numerator and denominator are more likely to occur. We keep only approximations with $\chi^2/\text{d.o.f.} < 2.5$. In `CalcSingularities(R_j)`, we determine the roots of the denominator of R_3^3 and check if they are canceled by poles in the numerator. For such cancellations we allow for a tolerance of $\Delta = 0.03$. Finally we calculate the mean and

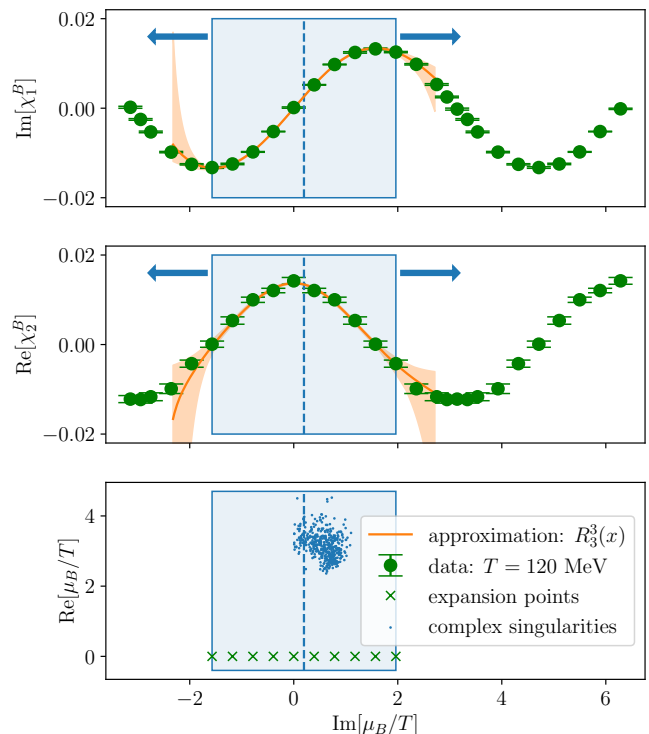


FIG. 5. A visualization of the sliding window analysis for $T = 120$ MeV. We show the data for χ_1^B (upper panel) and χ_2^B (middle panel) together with the rational approximation $R_3^3(\mu_B/T)$ obtained from the fit interval that is indicated by the blue box. The error band of the fit is obtained by Gaussian bootstrapping. The complex singularities obtained for each of the bootstrap samples are shown on the lower panel.

error for the singularities for which we chose the median and 1- σ percentile of the real and imaginary part. For the ellipses shown in Fig. 3 we also calculate the Pearson correlation coefficient. We repeat the sliding window analysis for each of the temperatures. The results for the real and imaginary parts of the singularities at the example of $T = 120$ MeV and $T = 136$ MeV are shown in Fig. 6.

Statistical analysis of fit results.—Next we perform scaling fits to equation (5). We chose one of the 55 intervals for each of the 5 different temperatures. This gives us 55^5 different data sets. In practice we chose $\mathcal{O}(10^5)$ random samples from possible interval combinations. The results for T^{CEP} and μ_B^{CEP} are summarized in Fig. 1 as a 2d-histogram. We also calculate the relative likelihood of each fit in accordance with the Akaike information criterion. In particular, we calculate the weights

$$w_{\text{AIC},j} = \frac{\exp\{(\text{AIC}_{\min} - \text{AIC}_j)/2\}}{\sum_j \exp\{(\text{AIC}_{\min} - \text{AIC}_j)/2\}}, \quad (9)$$

where index j labels the fits and $\text{AIC} = 2 \log \mathcal{L} = \chi^2$. We observe that models with small T^{CEP} or large μ_B^{CEP} are further suppressed when we weight the results with

$w_{\text{AIC},i}$. A one dimensional histogram of the T^{CEP} and μ_B^{CEP} results, respectively, is shown in Fig. 7. On top of the histograms we show standard box-and-whiskers diagrams for the data, where the vertical line inside the boxes indicates the median. Note that the size of the

box indicates here the interquartile range ($\text{IQR}=Q_3-Q_1$) and the whiskers have the length of $1.5 \cdot \text{IQR}$, except for $T > T^{\text{CEP}}$, where we indicate the maximal values that occur.

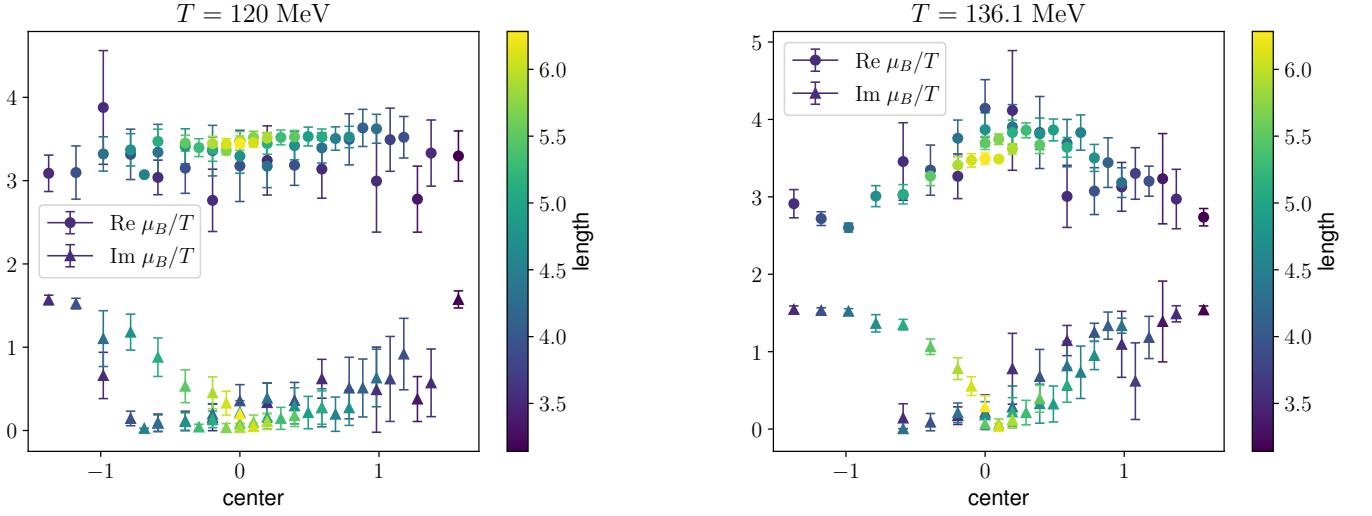


FIG. 6. Fit range dependence for the rational approximation $R_3^3(\mu_B/T)$ for $T = 120$ MeV (left) and $T = 136$ MeV (right). Shown are the real (circles) and imaginary (triangles) parts of the obtained poles vs. the center of the fit interval. The length of the fit interval is indicated by the color and varies from π to 2π .

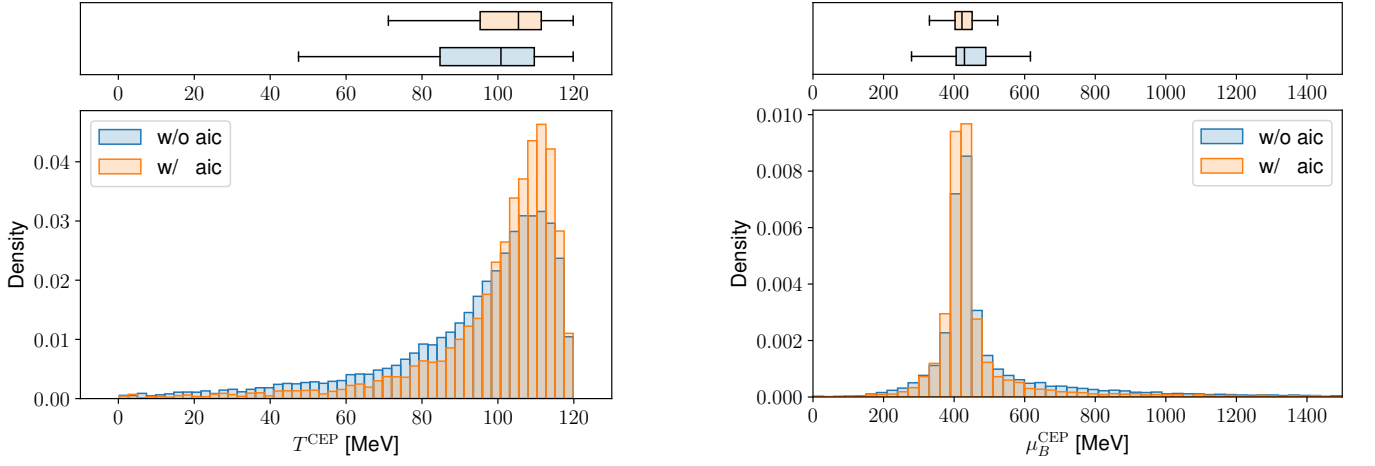


FIG. 7. Probability density of T^{CEP} (left) and μ_B^{CEP} (right) with standard boxplots on top of the data, based on $\mathcal{O}(10^5)$ individual fits of (5) to the positions of the LYE.